

Matched Filter-Based Molecule Source Localization in Advection-Diffusion-Driven Pipe Networks with Known Topology

Timo Jakumeit^{1,*}, Bastian Heinlein^{1,2,*}, Vukašin Spasojević¹, Vahid Jamali², Robert Schober¹, and Maximilian Schäfer¹

¹ Friedrich-Alexander-Universität Erlangen-Nürnberg (FAU), Erlangen, Germany

² Technical University of Darmstadt, Darmstadt, Germany

Abstract

Synthetic molecular communication (MC) has emerged as a powerful framework for modeling, analyzing, and designing communication systems where information is encoded into properties of molecules. Among the envisioned applications of MC is the localization of molecule sources in pipe networks (PNs) like the human cardiovascular system (CVS), sewage networks (SNs), and industrial plants. While existing algorithms mostly focus on simplified scenarios, in this paper, we propose the first framework for source localization in complex PNs with known topology, by leveraging the *mixture of inverse Gaussians for hemodynamic transport (MIGHT)* model as a closed-form representation for advection-diffusion-driven MC in PNs. We propose a matched filter (MF)-based approach to identify molecule sources under realistic conditions such as unknown release times, random numbers of released molecules, sensor noise, and limited sensor sampling rate. We apply the algorithm to localize a source of viral markers in a real-world SN and show that the proposed scheme outperforms randomly guessing sources even at low signal-to-noise ratios (SNRs) at the sensor and achieves error-free localization under favorable conditions, i.e., high SNRs and sampling rates. Furthermore, by identifying clusters of frequently confused sources, reliable cluster-level localization is possible at substantially lower SNRs and sampling rates.

1 Introduction

In the past years, synthetic molecular communication (MC) has emerged as a powerful framework for modeling, analyzing, and designing information exchange in systems where molecules act as information carriers, and numerous innovative applications within the human body [1], between plants [2], or in industrial environments have been envisioned [3–5].

One application that has attracted sustained interest is anomaly localization in MC systems [6]. Especially *molecule source localization*, i.e., the estimation of the location of a transmitter (Tx) emitting signaling molecules within an MC system, has proven particularly relevant for various application scenarios. In biomedical applications, source localization shall enable the localization of diseased tissue within the human body or more precisely, the

cardiovascular system (CVS), with the potential to identify pathologies much earlier than classical medical imaging techniques [1]. In epidemiological surveillance, source localization based on molecular signals in sewage networks (SNs) can support the early detection and spatial attribution of infections, offering a cost-effective alternative to population-wide testing [7]. In industrial systems, molecule source localization could provide a complementary approach for identifying leaks or contaminant releases in pipe networks (PNs) by exploiting concentration measurements of specific chemical species.

The aforementioned application domains span different size scales (see Fig. 1a) but share a common structural characteristic: they can be represented as PNs, i.e., networks of interconnected conduits through which molecules are transported by flowing liquids or gases. In the CVS, blood vessels form PNs carrying biomarkers, nutrients, and metabolic waste. In SNs, pipes transport wastewater and potential infection markers. In industrial gas or fluid networks, pipes convey process media, while released chemicals, pollutants, or tracers propagate through the PN and are detectable downstream. PNs thus represent a particularly important class of environments for molecule source localization. However, the structural features of PNs induce complex molecule transport dynamics. Therefore, accurate molecule source localization in PNs requires mathematical models that explicitly account for advection, diffusion, and the underlying network topology [8].

Most of the existing literature on molecule source localization in MC is focused on unbounded diffusion environments, and only a limited number of studies have considered source localization in single pipes or individual pipe branchings, where molecule propagation is governed by advection and diffusion. In [9], a one-dimensional (1-D) analytical source localization approach for a single pipe is presented, where the source (i.e., Tx) position is inferred via Tx-receiver (Rx) distance estimation. In [10], a 1-D analytical framework for cooperative abnormality detection and localization is proposed, in which mobile sensors propagate in a single pipe and release signaling molecules upon sensing an abnormality. In [11], a learning-based distance estimation approach for branched MC systems is proposed, where multiple Tx emit molecules that propagate by advection-only through a simple Y-shaped pipe topology towards the Rx. Recurrent neural networks are used to infer Tx-Rx distances from the received signal. In [12], a learning-based framework for infection source localization in the CVS is proposed. Using the BloodVoyagerS simulator, biomarkers released by static infection sources propagate through a PN of the major arteries via advection and subject to chemical degradation. Localization is formulated as a multi-class classification problem

*Both authors contributed equally to this work.

This work was funded in part by the German Federal Ministry of Research, Technology and Space (BMFT) through Project Internet of Bio-Nano-Things (IoBNT) – grant numbers 16KIS1987 and 16KIS1992, in part by the German Research Foundation (Deutsche Forschungsgemeinschaft, DFG) under GRK 2950 – ProjectID 509922606 and under grant number SCHA 2350/2-1, in part by the European Union’s Horizon Europe – HORIZON-EIC-2024-PATHFINDEROPEN-01 under grant agreement Project N. 101185661, and in part by the Horizon Europe Marie Skłodowska Curie Actions (MSCA)-UNITE under Project 101129618.

based on received biomarker signals using simulation data and stacked ensemble learning.

In summary, existing works on molecule source localization in MC predominantly consider highly simplified channel topologies and transport dynamics. Most approaches are limited to diffusion-only or advection-only models, with only a few studies accounting for their combined effects. Moreover, no existing works provide analytically tractable and physically interpretable localization frameworks that are applicable to PNs across different scales and different application scenarios. To overcome the drawbacks of existing approaches, we propose the first molecule source localization framework for advective-diffusive MC in PNs. Our approach builds on the *mixture of inverse Gaussians for hemodynamic transport (MIGHT)* model [13], which provides a closed-form description of molecule transport in PNs and is extended here to explicitly account for key system uncertainties, including unknown release times and quantities, sensor noise, and different sampling rates at the Rx. Based on this model, we develop a matched filter (MF)-based localization algorithm and demonstrate that clustering frequently confused Txs can significantly enhance localization performance on a cluster-level. The effectiveness of the proposed framework is illustrated by applying it for the localization of a source of viral markers in a real-world SN in the Zolkiewka Commune in Poland, highlighting its practical relevance and applicability.

The main contributions of this work are as follows:

- We extend the deterministic MIGHT channel model from [13] to account for log-normal-distributed random release quantities at the Txs and sensor noise at the Rx.
- We propose an MF-based algorithm for molecule source localization in advection-diffusion-driven PNs of arbitrary sizes and structural complexities.
- We introduce methods for the clustering of commonly confused Txs to improve cluster-level localization accuracy.
- We illustrate the accuracy of the proposed localization framework for different sensor sampling rates by its application for source localization in a real-world SN.

The remainder of the paper is organized as follows: Section 2 introduces the system model, reviews the MIGHT model, and presents the Rx noise model. Section 3 presents the MF-based localization approach and the Tx clustering method. Section 4 discusses numerical results, and Section 5 concludes the paper.

2 System and Channel Model

In the following, we first define PNs, then describe the assumptions on the molecule sources, i.e., Txs, including the randomness of the number of released molecules, and the advective-diffusive transport. Subsequently, we review the MIGHT channel model. Finally, we discuss the Rx model and the associated sensor noise.

2.1 Pipe Network Definition

To model molecule transport in PNs, we adopt the definition from [13] and approximate the PN topology using three segment types¹:

- (1) *Pipe*: A pipe p_i is a cylindrical conduit transporting fluid from its inlet to its outlet, with length l_i and radius r_i . Pipes

connect to other pipes, bifurcations, or junctions. The PN contains E pipes.

- (2) *Bifurcation*: A bifurcation b_m is a connection where one or more inflow pipe(s) split(s) into multiple outflow pipes. The set of its outflow pipes is denoted by $O(b_m)$. A PN contains B bifurcations.
- (3) *Junction*: A junction is a connection where multiple inflow pipes merge into one outflow pipe.

Bifurcations, junctions, inlet(s), outlet(s), and any connection point are modeled as nodes. We differentiate between three node types:

- (1) *Inlet node*: Inlet nodes $n_{in,a} \in \mathcal{N}_{in} = \{n_{in,1}, \dots, n_{in,I}\}$ with $I \in \mathbb{N}$ exist at the points of the PN where fluid flow is introduced into the PN. Here, \mathbb{N} denotes the set of natural numbers.
- (2) *Outlet node*: Outlet nodes $n_{out,b} \in \mathcal{N}_{out} = \{n_{out,1}, \dots, n_{out,O}\}$ with $O \in \mathbb{N}$ exist at the points of the PN where fluid flow leaves the PN.
- (3) *Connecting node*: All other $C \in \mathbb{N}$ points in the PN where pipes are connected to one another are referred to as connecting nodes $n_i \in \mathcal{N}_{con} = \{n_1, \dots, n_C\}$.

Pipes are represented as directed edges between nodes, aligned with the fluid flow direction, determined in Section 2.3. For any node type, the node at the inlet and outlet of a pipe p_i , i.e., the *source* and *destination node*, is denoted by $\mathcal{S}(p_i)$ and $\mathcal{D}(p_i)$, respectively².

The representation based on nodes and directed edges allows any PN to be described as a directed multigraph. The set of all distinct directed paths between a given (inlet/connecting) node $n_a \in \mathcal{N}_{in} \cup \mathcal{N}_{con}$ and another (connecting/outlet) node $n_b \in \mathcal{N}_{con} \cup \mathcal{N}_{out}$ is denoted by $\mathcal{P}(n_a, n_b)$. Each path P_k comprises a subset of pipes and bifurcations given by

$$P_k = \{p_i \mid i \in \mathcal{E}_k\} \cup \{b_m \mid m \in \mathcal{B}_k\}, \quad (1)$$

where $\mathcal{E}_k \subseteq \{1, \dots, E\}$ and $\mathcal{B}_k \subseteq \{1, \dots, B\}$ are the index sets of the pipes and bifurcations³ included in P_k . Any path must contain at least two pipes, i.e., $|\mathcal{E}_k| > 1$, where $|\cdot|$ denotes the cardinality.

2.2 Molecule Sources

We assume that there are U Txs. Any $\text{Tx}_g \in \mathcal{N}_{Tx} = \{\text{Tx}_1, \dots, \text{Tx}_U\}$ is a zero-dimensional (0-D) point at position $z_{\text{Tx}_g} \in [0, l_i]$ in pipe p_i . We denote the source node of pipe p_i containing Tx_g as $\mathcal{S}_{\text{Tx}}(\text{Tx}_g)$. Moreover, we assume that each Tx_g can impulsively release M_g molecules. Here, the number of released molecules M_g is modeled as a random variable (RV) with mean \bar{M}_g , realization m_g , and probability density function (PDF) $f_{M_g}(m_g)$, chosen according to the application scenario (see Section 4).

2.3 Advective-Diffusive Molecule Transport

In many practical PNs, including SNs, the CVS, and gas pipelines, see Fig. 1a), molecule transport is governed primarily by advection, i.e., transport with the bulk fluid motion, and diffusion, see Fig. 1b), encompassing both molecular and turbulent dispersive effects. We summarize the advective-diffusive transport assumptions underlying the proposed model below.

²Please refer to Figs. 1a) and 1c) in [13] for a visual illustration of the notation.

³Potential bifurcations at n_a or n_b are *excluded* from the set in (1), as molecules in any path from n_a and n_b do not travel *through* n_a or n_b , but start at n_a and end at n_b .

¹Please refer to Fig. 2a) in [13] for a visual illustration of the segment types.

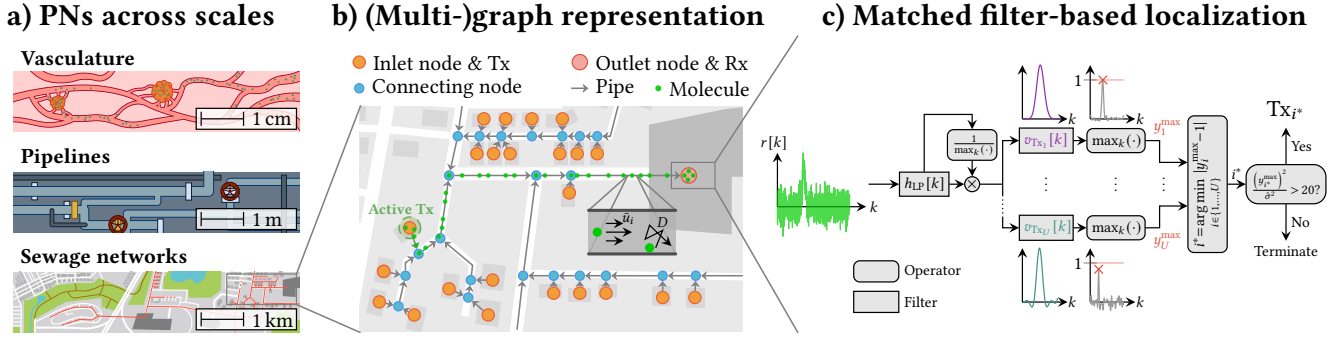


Figure 1: System model. a) Advection-diffusion-driven PNs across different scales. b) (Multi-)graph representation of a PN. c) MF bank-based molecule source localization algorithm, exploiting the MIGHT model for MF design.

Each inlet node $n_{in,a} \in \mathcal{N}_{in}$ is assigned a flow rate $Q_{in,a} > 0$, inducing flow in each pipe p_i in the PN, characterized by the flow rate Q_i and the cross-sectional average velocity $\bar{u}_i = Q_i/(\pi r_i^2)$ as determined using an equivalent electrical circuit model [13]. Additionally, molecules propagate via diffusion, characterized by the effective diffusion coefficient in pipe p_i [14, Eq. (26)]

$$\bar{D}_i = \frac{r_i^2 \bar{u}_i^2}{48D} + D, \quad (2)$$

where D denotes the diffusion coefficient.

2.4 MIGHT Channel Model

In this work, we adopt MIGHT [13] to model the PN. MIGHT exploits that the first passage times (FPTs) of molecules in advective-diffusive channels follow an inverse Gaussian (IG) distribution, and yields tractable, closed-form expressions for molecule transport in PNs, making it well-suited for applications that require a mathematically well-behaved framework, such as source localization [13]. Below, we briefly introduce the core equations of MIGHT.

2.4.1 Path Molecule Flux. Let $Tx_g \in \mathcal{N}_{Tx}$ be at position z_{Tx_g} in pipe p_q and let the Rx be at position z_{Rx} in pipe p_w . Moreover, any path contained in $\{P_k \in \mathcal{P}(\mathcal{S}_{Tx}(Tx_g), \mathcal{D}(p_w)) | p_q, p_w \in P_k\}$ leads from Tx_g to the Rx and contains pipes p_q and p_w . Then, the molecule flux observed at the Rx position z_{Rx} in pipe p_w due to the release of $m_g = 1$ molecule at Tx_g follows an IG distribution and is obtained in s^{-1} as [13, Eqs. (8), (14), (15), (17)]

$$\bar{j}_k(z_{Rx}; z_{Tx_g}, t) = \frac{\bar{\mu}_k(z_{Rx}; z_{Tx_g})}{\sqrt{2\pi\bar{\theta}_k(z_{Rx}; z_{Tx_g})t^3}} \exp\left(-\frac{(t - \bar{\mu}_k(z_{Rx}; z_{Tx_g}))^2}{2\bar{\theta}_k(z_{Rx}; z_{Tx_g})t}\right), \quad (3)$$

with mean, variance, and scale parameter of path P_k given by [13, Eq. (15), (16), (17)]

$$\bar{\mu}_k(z_{Rx}; z_{Tx_g}) = \mu_q(l_q - z_{Tx_g}) + \mu_w(z_{Rx}) + \sum_{i \in \mathcal{E}_k \setminus \{q,w\}} \mu_i(l_i), \quad (4)$$

$$\bar{\sigma}_k^2(z_{Rx}; z_{Tx_g}) = \sigma_q^2(l_q - z_{Tx_g}) + \sigma_w^2(z_{Rx}) + \sum_{i \in \mathcal{E}_k \setminus \{q,w\}} \sigma_i^2(l_i), \quad (5)$$

$$\bar{\theta}_k(z_{Rx}; z_{Tx_g}) = \frac{\bar{\sigma}_k^2(z_{Rx}; z_{Tx_g})}{\bar{\mu}_k(z_{Rx}; z_{Tx_g})}, \quad (6)$$

and mean and variance of pipe p_i given by [13, Eq. (7)]

$$\mu_i(z_i) = \frac{z_i}{\bar{u}_i}, \quad \sigma_i^2(z_i) = \frac{2\bar{D}_i z_i}{\bar{u}_i^3}, \quad (7)$$

where $z_i \in [0, l_i]$ denotes the longitudinal position within pipe p_i .

2.4.2 Channel Impulse Response. Given the path molecule flux in (3), the channel impulse response (CIR) between Tx_g and position z_{Rx} in pipe p_w in s^{-1} is obtained by summing up the weighted path fluxes of all paths between Tx_g and the Rx [13, Eq. (19)], i.e.,

$$h_{Tx_g, w}(z_{Rx}, t; z_{Tx_g}) = \sum_{\{P_k \in \mathcal{P}(\mathcal{S}_{Tx}(Tx_g), \mathcal{D}(p_w)) | p_q, p_w \in P_k\}} \gamma_{P_k} \bar{j}_k(z_{Rx}, t; z_{Tx_g}), \quad (8)$$

where the fraction of molecules γ_{P_k} propagating through path P_k is given as [1, Eq. (22)]

$$\gamma_{P_k} = \prod_{\substack{p_i, b_m \in P_k, \\ p_i \in \mathcal{O}(b_m)}} \frac{Q_i}{\sum_{p_v \in \mathcal{O}(b_m)} Q_v}. \quad (9)$$

2.5 Receiver Model

In this work, we focus on localization based on the signal received at a single sensor, i.e., Rx. We model the sensor as a transparent molecule counting Rx positioned in pipe p_w and characterized by its length $l_{Rx} \in (0, l_w]$ and its longitudinal center position $z_{Rx} \in [0 + l_{Rx}/2, l_w - l_{Rx}/2]$. Then, assuming the advective flux in pipe p_w dominates the diffusive flux, the expected number of molecules at the Rx due to a release of M_g molecules at Tx_g follows as [13, Eqs. (23), (24)]

$$\begin{aligned} N_{Rx, Tx_g}(t) &= \frac{M_g}{\bar{u}_w} \int_{z_{Rx} - l_{Rx}/2}^{z_{Rx} + l_{Rx}/2} h_{Tx_g, w}(z_w, t; z_{Tx_g}) dz_w \\ &\approx \frac{M_g l_{Rx}}{\bar{u}_w} h_{Tx_g, w}(z_{Rx}, t; z_{Tx_g}), \end{aligned} \quad (10)$$

where the latter approximation is valid under the uniform concentration assumption (UCA).

In practice, the Rx does not have access to time-continuous molecule counts $N_{Rx, Tx_g}(t)$. Instead it obtains every T_s seconds a noisy sample of $N_{Rx, Tx_g}(t)$, which is inherently band-limited. In this paper, we neglect channel-induced counting noise in (11), as $N_{Rx, Tx_g}(t)$ will be typically very large and thus counting noise will be negligible [8]. However, we assume that the k -th sample is analyzed by a sensor which is subject to noise $N_s[k]$, where $N_s[k]$

is modeled as zero-mean additive white Gaussian noise (AWGN) with variance σ_s^2 . Considering this model, where the sensor noise power is independent of the sampling frequency $f_s = 1/T_s$, we arrive at the following expression for the sensor response

$$r[k] = N_{\text{Rx},\text{Tx}_g}(kT_s) + N_s[k] := N_{\text{Rx},\text{Tx}_g}[k] + N_s[k]. \quad (11)$$

3 Molecule Source Localization

We consider source localization in PNs with multiple Txs and a single Rx, where exactly one *active* Tx, Tx_g , emits molecules in a single impulsive release⁴, see Fig. 1b). While the PN topology and all Tx positions are known, the active Tx_g is *unknown*, and localization is defined as identifying it based on the received signal in (11).

3.1 Matched Filter Bank Algorithm

We propose an MF-based algorithm that aims to distinguish between individual Txs based on the received signal by exploiting the known CIR in (8) between any Tx and the Rx, see Fig. 1c).

3.1.1 Signal Pre-Processing. For a single active Tx_g releasing M_g molecules, the discrete expected number of molecules arriving at the Rx in sampling interval k is given as $N_{\text{Rx},\text{Tx}_g}[k]$, see (10). Since M_g is an RV whose realization is unknown at the Rx and may vary over several orders of magnitude [15, 16], the amplitude of the received signal in (11) cannot be reliably exploited for localization, see Figs. 3c) and 3d). Normalizing the received signal by its maximum value helps to mitigate this problem, but due to the AWGN at the Rx, it is not possible to know the exact signal maximum. Therefore, the received signal is first filtered with a low-pass (LP) filter $h_{\text{LP}}[k]$, whose cut-off frequency is chosen based on the frequency contents of the known CIRs, resulting in the filtered received signal

$$r_{\text{LP}}[k] = r[k] * h_{\text{LP}}[k] \stackrel{(11)}{=} \underbrace{N_{\text{Rx},\text{Tx}_g}[k] * h_{\text{LP}}[k]}_{:= N_{\text{Rx},\text{Tx}_g,\text{LP}}[k]} + \underbrace{N_s[k] * h_{\text{LP}}[k]}_{:= N_{s,\text{LP}}[k]}, \quad (12)$$

where $*$ denotes convolution with respect to time, and $N_{\text{Rx},\text{Tx}_g,\text{LP}}[k]$ and $N_{s,\text{LP}}[k]$ are the LP-filtered signal and sensor noise components of $r_{\text{LP}}[k]$, respectively. Afterwards, $r_{\text{LP}}[k]$ is normalized by its maximum value, which is now much less impacted by noise, yielding an LP-filtered, normalized version of the received signal

$$\tilde{r}_{\text{LP}}[k] = \frac{r_{\text{LP}}[k]}{\max_k(r_{\text{LP}}[k])}. \quad (13)$$

The normalization of the received signal removes all information about the number of emitted molecules in $r_{\text{LP}}[k]$.

3.1.2 Matched Filter Design. The signal used to construct the MF for a given Tx_g does not rely directly on the noisy received signal in (11). Rather, it is calculated using the analytical channel model in (10). Since the MF is applied *after* the LP filtering of the received signal, in the first step of the MF design, the number of observed molecules in (10) is LP-filtered with the same filter $h_{\text{LP}}[k]$ as in (12). This yields the LP-filtered expected number of molecules $N_{\text{Rx},\text{Tx}_g,\text{LP}}[k]$ arriving at the Rx (see also (12)). To account for the normalization of the received signal in (13), we also normalize the

⁴The latter assumption is justified in cases where emissions at the active Tx are rare.

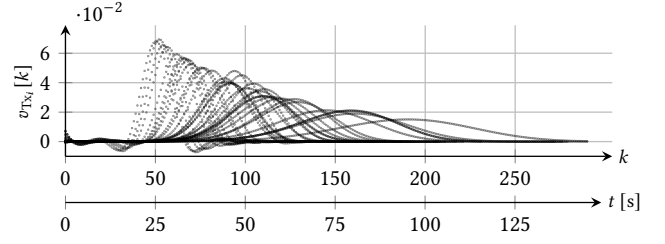


Figure 2: MFs $v_{\text{Tx}_i}[k]$ used for source localization in the PN shown in Fig. 3a) with $U = 33$ Txs at a sensor sampling frequency of $f_s = 2$ Hz.

expected number of molecules by its maximum value, i.e.,

$$\tilde{N}_{\text{Rx},\text{Tx}_g,\text{LP}}[k] = \frac{N_{\text{Rx},\text{Tx}_g,\text{LP}}[k]}{\max_k(N_{\text{Rx},\text{Tx}_g,\text{LP}}[k])}. \quad (14)$$

Because we use an LP filter in (12), the originally white sensor noise becomes colored. To ensure the MF accounts for this, we first compute the colored noise autocorrelation function (ACF) as

$$R_{nn}[k] = \sigma_s^2 \delta[k] * h_{\text{LP}}[k] * h_{\text{LP}}[-k] = \sigma_s^2 h_{\text{LP}}[k] * h_{\text{LP}}[-k], \quad (15)$$

where $\delta[k]$ denotes the Kronecker delta function. From the ACF in (15), the colored noise autocorrelation matrix follows as a Toeplitz matrix [17]

$$\mathbf{R}_{nn} = \begin{bmatrix} R_{nn}[0] & R_{nn}[1] & R_{nn}[2] & \cdots & R_{nn}[M-1] \\ R_{nn}[1] & R_{nn}[0] & R_{nn}[1] & \cdots & R_{nn}[M-2] \\ \vdots & \vdots & \vdots & \ddots & \vdots \\ R_{nn}[M-1] & R_{nn}[M-2] & R_{nn}[M-3] & \cdots & R_{nn}[0] \end{bmatrix}. \quad (16)$$

Next, we represent the expected, LP-filtered, and normalized signal $\tilde{N}_{\text{Rx},\text{Tx}_g,\text{LP}}[k]$ as a vector of finite length whose elements are the sampled signal values, i.e.,

$$\tilde{\mathbf{N}}_{\text{Rx},\text{Tx}_g,\text{LP}} = [\tilde{N}_{\text{Rx},\text{Tx}_g,\text{LP}}[0], \dots, \tilde{N}_{\text{Rx},\text{Tx}_g,\text{LP}}[M-1]]^\top, \quad (17)$$

where $(\cdot)^\top$ denotes the transpose operator and M is chosen large enough such that the expected signal has decayed to zero.

Finally, the MF for Tx_g is⁵ a vector of length M [18, Eq. (9.19)]

$$\mathbf{v}_{\text{Tx}_g} = \frac{\mathbf{R}_{nn}^{-1} \tilde{\mathbf{N}}_{\text{Rx},\text{Tx}_g,\text{LP}}}{\tilde{\mathbf{N}}_{\text{Rx},\text{Tx}_g,\text{LP}}^\top \mathbf{R}_{nn}^{-1} \tilde{\mathbf{N}}_{\text{Rx},\text{Tx}_g,\text{LP}}}, \quad g \in \{1, \dots, U\}, \quad (18)$$

where the numerator maximizes the signal-to-noise ratio (SNR) for the received signal from Tx_g , and the denominator is a normalization scalar ensuring a maximum MF output amplitude of 1 when convolved with the corresponding received signal. We denote the k -th element of the MF as $v_{\text{Tx}_g}[k]$, $k \in \{0, \dots, M-1\}$. See Fig. 2 for exemplary MFs. Negative values arise from the LP filtering in (12).

3.1.3 Matched Filtering of Received Signal. To perform the matched filtering, we collect for all time steps in the observation interval the past M samples of the LP-filtered, normalized received signal $\tilde{r}_{\text{LP}}[k]$ in a vector $\tilde{\mathbf{r}}_{\text{LP}}[k]$ according to

$$\tilde{\mathbf{r}}_{\text{LP}}[k] = [\tilde{r}_{\text{LP}}[k], \dots, \tilde{r}_{\text{LP}}[k-M+1]]^\top. \quad (19)$$

⁵The MF design in (18) is motivated by radar signal processing [18], where such filters are known as *Capon* or *Minimum Variance Distortionless Response (MVDR)* beamformers. The Tx decision rule in (21) is motivated by the same framework.

To identify the active Tx, the signal in (19) is filtered by a filter bank comprising the MFs of all Txs for all time steps in the observation interval, i.e.,

$$y_i[k] = \mathbf{v}_{\text{Tx}_i}^\top \tilde{\mathbf{r}}_{\text{LP}}[k], \quad i \in \{1, \dots, U\}. \quad (20)$$

Then, the Tx whose MF output has the maximum amplitude closest to 1, denoted by Tx_{i^*} , is selected as the candidate active Tx, i.e.,

$$i^* = \arg \min_i |y_i^{\max} - 1|, \quad y_i^{\max} = \max_k (y_i[k]), \quad i \in \{1, \dots, U\}. \quad (21)$$

Lastly, to prevent pure noise at the Rx from being misidentified as a signal, the ratio of the peak power to noise variance, $(y_{i^*}^{\max})^2 / \hat{\sigma}^2$ is computed for the MF output corresponding to the candidate active Tx. The noise variance $\hat{\sigma}^2$ is estimated within an observation window around the peak, where samples are included only once their amplitude drops below 10% of the peak amplitude.

3.1.4 Basic Localization Algorithm. The individual steps of the localization algorithm are illustrated in Fig. 1c). The received signal is first passed through an LP filter, see (12), and then normalized by its maximum value, see (13). Subsequently, an MF bank comprising the MFs of all Txs, see (20), is applied. Finally, the MF whose maximum output is closest to 1 is identified, see (21), and the Tx corresponding to this filter is declared as the localized source only if the peak power to noise variance ratio surpasses a threshold. For our simulations, we have set this threshold to be equal to 20.

3.2 Clustering Likely Confused Sources

Localization based on an MF bank performs well when the received signals associated with different Txs exhibit sufficiently distinct temporal *shapes*. However, depending on the PN topology and the spatial proximity of the Txs, signals from different Txs may have highly similar shapes, see Section 4. In such cases, it can be advantageous to group Txs with similar CIRs into clusters and perform localization at a cluster-level, where localization is considered successful if the estimated Tx belongs to the same cluster as the active Tx. Although this approach may not identify the exact active Tx, it narrows the set of prospective Txs to a small subset of all Txs.

In this work, clustering is performed using the Louvain community detection algorithm [19] applied to a graph whose nodes represent all Txs in the PN and whose edge weights quantify the similarity between their corresponding CIRs. This similarity graph can be constructed either empirically from the confusion matrix (CM) or analytically from the cosine similarity matrix (CSM). Because the Louvain algorithm chooses clusters that maximize *modularity*, a measure for how well a graph is separated into tightly-knit groups, it groups very similar CIRs together as these have high edge weights. In the following, we describe the construction of the CM and CSM, and the subsequent evaluation of the clustering.

3.2.1 Confusion Matrix. The CM is denoted by $\text{CM} \in [0, 1]^{U \times U}$. It is constructed by applying the localization algorithm in Section 3.1.4 N_{sim} times for each $\text{Tx}_i \in \mathcal{N}_{\text{Tx}}$, using independent noisy realizations of the received signal in (11). After a total of $U \cdot N_{\text{sim}}$ runs, the entry $\text{CM}_{ij} \in [0, 1]$ of CM represents the fraction of simulation runs where, instead of the active Tx_i , Tx_j was classified as the signal source. Entries on the main diagonal represent the fractions of simulation runs where the active Tx was correctly identified.

We find that binarizing CM reduces variability across simulation runs and improves clustering quality (see Section 3.2.3). The binarized matrix CM^b is obtained by setting entries with fewer than 5% confusions to zero and all others to one, i.e.,

$$\text{CM}_{ij}^b = \begin{cases} 1, & \text{if } \text{CM}_{ij} \geq 0.05 \\ 0, & \text{if } \text{CM}_{ij} < 0.05 \end{cases}. \quad (22)$$

Matrix CM^b is interpreted as a directed graph, on which the Louvain community detection algorithm [19] is applied to obtain clusters.

3.2.2 Cosine Similarity Matrix. Contrary to the CM, the CSM, denoted by $\text{CSM} \in [0, 1]^{U \times U}$, does not rely on empirical simulations. It is given by the pairwise cosine similarities of the Tx CIRs, i.e.,

$$\text{CSM}_{ij} = \frac{\int_{-\infty}^{\infty} h_{\text{Tx}_i, w}(z_{\text{Rx}}, t; z_{\text{Tx}_i}) h_{\text{Tx}_j, w}(z_{\text{Rx}}, t; z_{\text{Tx}_j}) dt}{\sqrt{\int_{-\infty}^{\infty} h_{\text{Tx}_i, w}^2(z_{\text{Rx}}, t; z_{\text{Tx}_i}) dt} \sqrt{\int_{-\infty}^{\infty} h_{\text{Tx}_j, w}^2(z_{\text{Rx}}, t; z_{\text{Tx}_j}) dt}}. \quad (23)$$

Binarization is performed similarly as for the CM, with an adjusted threshold, as the cosine similarity metric assigns values close to one for similar signals, i.e.,

$$\text{CSM}_{ij}^b = \begin{cases} 1, & \text{if } \text{CSM}_{ij} \geq 0.95 \\ 0, & \text{if } \text{CSM}_{ij} < 0.95 \end{cases}. \quad (24)$$

Note that CSM^b is symmetric and is interpreted as an undirected graph in the Louvain community algorithm [19], which is applied to obtain clusters of likely confused Txs.

3.2.3 Clustering Quality. Txs are considered well clustered if CIRs within each cluster are highly similar, while differing significantly across different clusters. To quantify clustering quality, we employ the silhouette score [20] based on the squared Euclidean distance, denoted by $\|\cdot\|_2$, between the normalized CIRs, i.e.,

$$d(\text{Tx}_i, \text{Tx}_j) = \left\| \tilde{h}_{\text{Tx}_i, w}(z_{\text{Rx}}, t; z_{\text{Tx}_i}) - \tilde{h}_{\text{Tx}_j, w}(z_{\text{Rx}}, t; z_{\text{Tx}_j}) \right\|_2^2, \quad (25)$$

$$\text{with } \tilde{h}_{\text{Tx}_i, w}(z_{\text{Rx}}, t; z_{\text{Tx}_i}) = \frac{h_{\text{Tx}_i, w}(z_{\text{Rx}}, t; z_{\text{Tx}_i})}{\max_t (h_{\text{Tx}_i, w}(z_{\text{Rx}}, t; z_{\text{Tx}_i}))}. \quad (26)$$

The silhouette score ranges from -1 to 1 , with higher values indicating compact, well-separated clusters and lower values reflecting poor clustering quality. To compare the similarity of the clustering results obtained from CM^b and CSM^b , we use the adjusted rand index (ARI) [21, Eq. (21)], ranging from -0.5 to 1 , where a value of 1 indicates identical clustering based on CM^b and CSM^b .

4 Results

To investigate the performance of the proposed localization approaches, we first introduce a real-world SN as an exemplary application domain and then assess the localization performance.

4.1 Sewage Pipe Network

We simulate part of a SN in the Zolkiewka Commune, Poland [22], as shown in Fig. 3a). We make the following simplifying assumptions: Each house connected to the sewage system is modeled as an inlet node $n_{\text{in},g}$ with a constant inflow rate $Q_{\text{in},g} = 5 \times 10^{-3} \text{ m}^3 \text{ s}^{-1}$, resulting in realistic flow rates within the PN, see Fig. 3a). At each inlet $n_{\text{in},g}$, a potentially active Tx_g is placed at $z_{\text{Tx}_g} = 0$, representing a source of viral markers. Molecule transport in the SN is

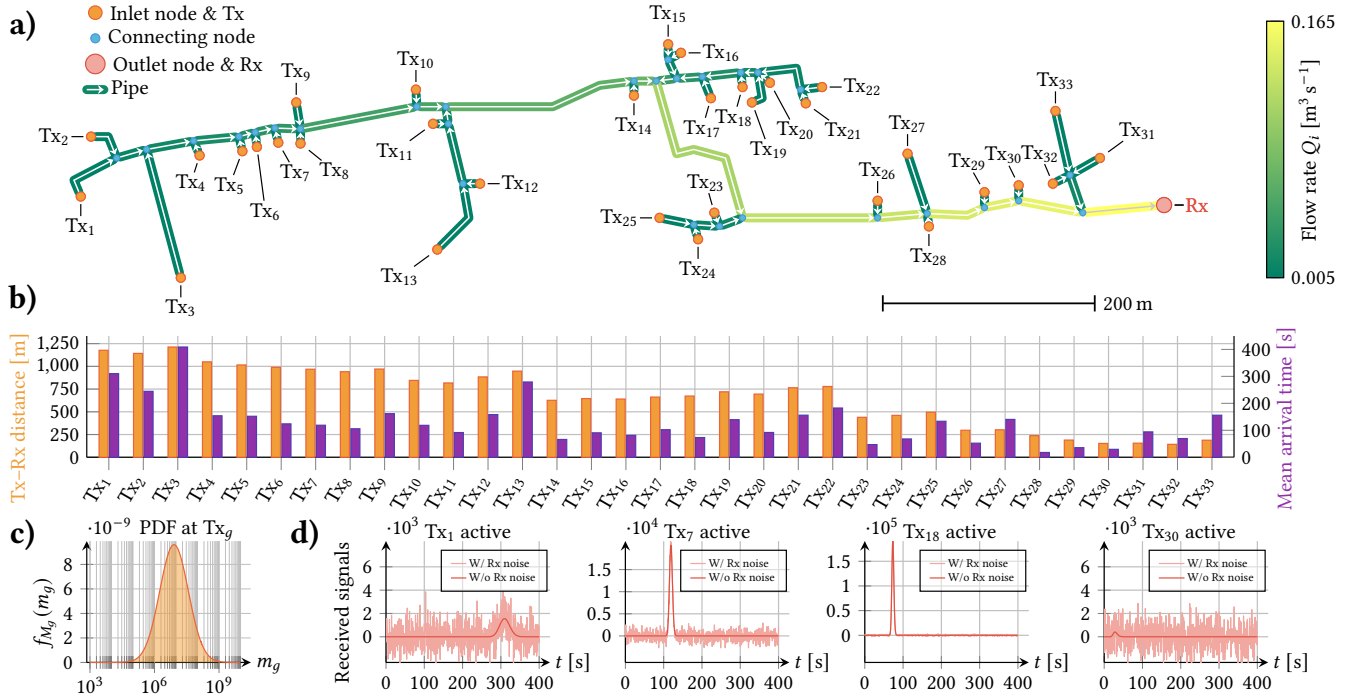


Figure 3: a) Topology of a SN in Zolkiewka Commune, Poland [22]. Pipe lengths l_i are drawn to scale (see scale bar) and $r_i = 5.5$ cm, $\forall p_i$. Inlet, connecting, and outlet node positions are illustrated in orange, blue, and red, respectively. At each inlet node $n_{in,g} \in \mathcal{N}_{in}$, a Tx_g is present with $Q_{in,g} = 5 \times 10^{-3}$ m³ s⁻¹. Flow directions are given by arrows, flow rates are color-coded in the edge colors. The Rx is located at the outlet node. b) Tx-Rx distances (orange) and Tx-Rx path mean arrival times (purple) for all Txs. c) Log-normal PDF for the number of released viral particles M_g at the active Tx_g . d) Four exemplary received signals from different active Txs with and without additive Rx noise.

assumed to be advection-diffusion-driven with diffusion coefficient $D = 0.2$ m² s⁻¹ [23], while gravitational effects and half-filled pipes typical of SNs are neglected [22].

At the active Tx_g , we assume a single impulsive release of viral markers. The number of released markers, denoted by M_g , is modeled as log-normally distributed, i.e., $\ln(M_g) \sim \mathcal{N}(\mu_{Tx}, \sigma_{Tx}^2)$, with mean $\mu_{Tx} = 18.69$ and variance $\sigma_{Tx}^2 = 2.46$ [15, 16], see Fig. 3c).

At the Rx, a default sampling rate of $f_s = 2$ Hz and noise power $\sigma_s^2 = 10^3$ are assumed. We emphasize that MIGHT serves as a simplified proxy for sewage transport, as our focus is on generic localization techniques in PNs rather than high-fidelity SN modeling.

4.2 Simulation Results

Below, we first present results on the CM and CSM and investigate the Tx clustering. Subsequently, we illustrate the localization accuracy for various sensor noise powers and sampling frequencies.

4.2.1 Transmitter Confusion Matrix and Cosine Similarity Matrix. Due to the similarity of the temporal shapes of the received signals associated with different Txs, see Fig. 5, several Tx pairs are likely confused by the localization algorithm in Section 3.1.4. For $N_{sim} = 100$ simulation runs per Tx, the resulting confusion rates are shown in Fig. 4 using the CM (left) and its binarized version (middle). In the CM, the observed confusion rates off the main diagonal range from 0% to 36%, with particularly high confusions between Tx_8 and Tx_{28} (36%). Note that CM^b is approximately symmetric.

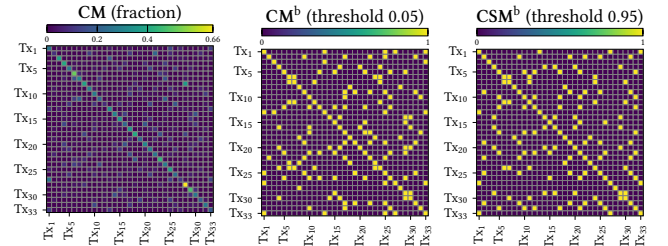
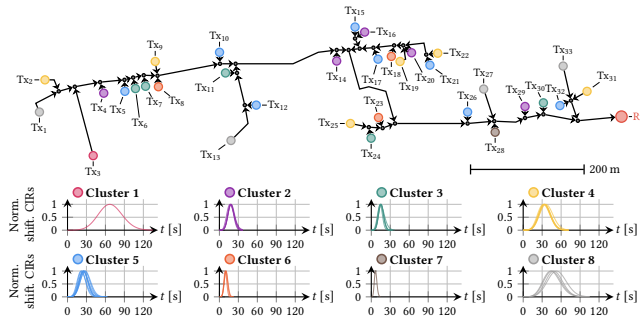


Figure 4: Likely confused Txs, illustrated using the empirically determined CM (left) and its binarized version (middle). Confusions predicted by the binarized CSM are shown on the right.

The right plot in Fig. 4 shows the confusions predicted by CSM^b . The agreement between clustering based on CM^b and two other clustering methods is quantified in Table 1 using the ARI, while clustering quality is evaluated via the silhouette score in (25). Both clustering methods based on CM^b and CSM^b yield good silhouette scores (0.49 and 0.60, respectively). Moreover, CM^b and CSM^b show good agreement (ARI = 0.70), confirming that the CSM is a useful proxy for the actual CM. As a baseline, we include K-means clustering based on the path means $\bar{\mu}_g$, with the number of clusters set equal to that obtained with the CM^b and CSM^b methods. Compared to these approaches, K-means yields poorer clusters (silhouette score -0.2763) and does not agree with the CM (ARI = -0.0053).

Table 1: Clustering evaluation metrics.

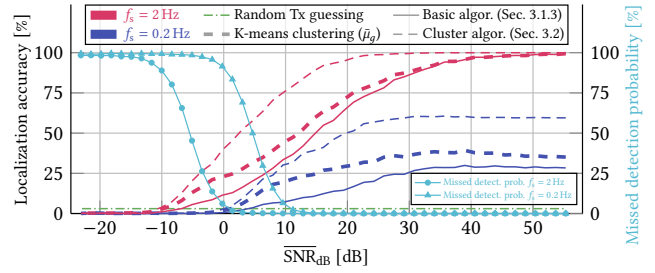
Clustering	Silhouette score	ARI
CM ^b	0.49	1.00
CSM ^b	0.60	0.70
K-means ($\bar{\mu}_g$)	-0.2763	-0.0053


Figure 5: Spatial distribution of Tx clusters. Below the SN, the normalized and time-shifted CIRs of all clusters are shown.

4.2.2 Spatial Spread of Source Clusters. In the top part of Fig. 5, the cluster assignment of each Tx is indicated by its color, as determined using CSM^b in (24). The bottom part shows the normalized and time-shifted CIRs of all Txs within each cluster. The time shift accounts for the unknown emission time at the Tx. Interestingly, while the CIRs of Txs within a cluster are very similar, the corresponding Txs are often not geographically close. This is because many parts of the SN exhibit heterogeneous flow rates in their immediate neighborhood, see Fig. 3a), leading to strongly varying CIRs of the Txs in these neighborhoods. This can also be observed in Fig. 3b), where it becomes clear that the Tx-Rx distances are not necessarily correlated to mean arrival times, due to varying flow rates. This has direct implications when using an MF-based localization algorithm to identify, e.g., an infected individual in a community. Investigating only the members of the identified household and geographically neighboring households is insufficient. Instead, households that are *close* in terms of molecule propagation time to the Rx must be considered, as the molecule release time is not known.

4.2.3 Localization Accuracy. Firstly, in Fig. 6, we show the localization accuracy of the MF-based localization algorithm proposed in Section 3.1.4 as a function of the SNR for both a sampling rate of $f_s = 2$ Hz (pink solid line) and $f_s = 0.2$ Hz (blue solid line). For this algorithm, the localization accuracy is defined as the percentage of simulation runs in which the active Tx is correctly identified. Secondly, Fig. 6 shows the localization accuracy for the CSM-based clustering approach in Section 3.2 for both sampling rates (thin dashed pink and blue lines) and clustering baselines based on K-means clustering (thick dashed pink and blue lines). In this setting, the localization accuracy is defined as the percentage of simulation runs in which the identified Tx lies within the cluster containing the active Tx. Thirdly, Fig. 6 shows the missed detection probability computed from the simulation runs (cyan solid lines), i.e., the probability that a signal is confused with noise and no localization is performed, which only depends on the sampling rate and the SNR.

The SNR is obtained by first calculating, for each Tx, the ratio between the expected received signal's (10) average power (using


Figure 6: Localization accuracy of the proposed algorithms and missed detection probability at different sensor sampling rates.

the mean number of released molecules \bar{M}_g) and the sensor noise power, and then averaging over all U Txs in the PN, i.e.,

$$\overline{\text{SNR}}_{\text{dB}} = 10 \log_{10} \left(\frac{1}{U} \sum_{\text{Tx}_g \in \mathcal{N}_{\text{Tx}}} \frac{\frac{1}{t_g^2 - t_g^1} \int_{t_g^1}^{t_g^2} N_{\text{Rx}, \text{Tx}_g}^2(z_{\text{Rx}}, t; z_{\text{Tx}_g}) dt}{\sigma_s^2} \right), \quad (27)$$

where $[t_g^1, t_g^2]$ represents the time interval during which the signal of Tx_g carries most of its energy. In our simulations, $\overline{\text{SNR}}_{\text{dB}}$ is varied by varying the sensor noise power σ_s^2 .

Starting with the sensor with sampling frequency $f_s = 2$ Hz (pink lines), the basic algorithm outperforms random guessing (green line, accuracy $1/U = 1/33$) already at $\overline{\text{SNR}}_{\text{dB}} = -10$ dB. For lower SNRs, the algorithm cannot distinguish signal from noise and thus fails to detect any Txs, resulting in large missed detection probabilities (cyan line with round markers) and zero correct identifications. As the SNR increases, the algorithm eventually achieves perfect localization accuracy. When considering the ability to predict the correct cluster (thin pink dashed line), we observe a gain of more than 10 dB compared to predicting the exact Tx (pink solid line), confirming the intuition from Section 3.2 that most confusions occur in small clusters of Txs. Moreover, at both sampling rates, the clustering algorithm from Section 3.2 (thin dashed lines) outperforms the algorithm based on K-means clustering (thick dashed lines). At the lower sampling rate of $f_s = 0.2$ Hz (blue lines), both the basic and clustering algorithms achieve significantly lower accuracy than for $f_s = 2$ Hz. This is due to two effects: the missed detection probability shifts by ~ 10 dB to the right (see cyan lines), and even when it reaches zero, perfect localization accuracy cannot be achieved independent of the SNR, since only limited information about the signal shape can be recovered at lower sampling rates.

5 Conclusion

In this work, we proposed the first analytical framework for molecule source localization in advection-diffusion-driven PNs with known topology based on the MIGHT channel model. The proposed MF-based approach reliably identifies a single active Tx among multiple known Txs from the signal of a single Rx, as illustrated for a model of a real-world SN. Furthermore, frequently confused Txs can be grouped into clusters that remain reliably distinguishable, drastically reducing the number of Txs requiring manual inspection in, e.g., epidemiological applications. Future work will study the transferability of the framework beyond SNs across application domains and scales, and investigate inter-Tx interference and experimental validation in branched MC testbeds.

References

- [1] Reza Mosayebi et al. Early cancer detection in blood vessels using mobile nanosensors. *IEEE Trans. NanoBiosci.*, 18:103–116, April 2019.
- [2] Bige D. Unluturk and Ian F. Akyildiz. An end-to-end model of plant pheromone channel for long range molecular communication. *IEEE Trans. NanoBiosci.*, 16(1): 11–20, 2017.
- [3] Luca Felicetti et al. Applications of molecular communications to medicine: A survey. *Nano Commun. Netw.*, 7:27–45, 2016.
- [4] Nariman others Farsad. A comprehensive survey of recent advancements in molecular communication. *IEEE Commun. Surv. Tutor.*, 18(3):1887–1919, 2016.
- [5] Dadi Bi et al. A survey of molecular communication in cell biology: Establishing a new hierarchy for interdisciplinary applications. *IEEE Commun. Surv. Tutor.*, 23(3):1494–1545, 2021.
- [6] Ali Etemadi et al. Abnormality detection and localization schemes using molecular communication systems: A survey. *IEEE Access*, 11:1761–1792, 2023.
- [7] Yu Deng et al. Use of sewage surveillance for COVID-19 to guide public health response: A case study in Hong Kong. *Sci. Total Environ.*, 821:153250, 2022.
- [8] Timo Jakumeit, Lukas Brand, Jens Kirchner, Robert Schober, and Sebastian Lotter. Vessel network topology in molecular communication: Insights from experiments and theory. *arXiv preprint arXiv:2512.02811*, December 2025.
- [9] Meriç Turan et al. Transmitter localization in vessel-like diffusive channels using ring-shaped molecular receivers. *IEEE Commun. Lett.*, 22(12):2511–2514, 2018.
- [10] Ladan Khalooupour et al. Theoretical concept study of cooperative abnormality detection and localization in fluidic-medium molecular communication. *IEEE Sens. J.*, 21(15):17118–17130, August 2021.
- [11] Martin Schottlender, Maximilian Schäfer, and Ricardo A. Veiga. Neural network-based distance estimation for branched molecular communication systems. In *Proc. 12th Annu. ACM Int. Conf. Nanoscale Comput. Commun.*, pages 28–33, 2025.
- [12] Saswati Pal et al. Machine learning-driven localization of infection sources in the human cardiovascular system. *IEEE Trans. Mol. Biol. Multi-Scale Commun.*, 11(4):524–530, 2025.
- [13] Timo Jakumeit, Bastian Heinlein, Nunzio Tuccitto, Robert Schober, Sebastian Lotter, and Maximilian Schäfer. Mixture of Inverse Gaussians for Hemodynamic Transport (MIGHT) in multiple input multiple output vascular networks. *arXiv preprint arXiv:2510.11743v2*, February 2026.
- [14] Rutherford Aris. On the dispersion of a solute in a fluid flowing through a tube. *Proc. R. Soc. (London) A*, 235:67–77, April 1956.
- [15] P. Foladori et al. SARS-CoV-2 from faeces to wastewater treatment: What do we know? A review. *Sci. Total Environ.*, 743:140444, 2020.
- [16] C. Rose, A. Parker, B. Jefferson, and E. Cartmell. The characterization of feces and urine: A review of the literature to inform advanced treatment technology. *Crit. Rev. Environ. Sci. Technol.*, 45(17):1827–1879, 2015.
- [17] Monson H. Hayes. *Statistical Digital Signal Processing and Modeling*. Wiley, 1996.
- [18] Mark A. Richards. *Fundamentals of Radar Signal Processing*. McGraw-Hill Electronic Engineering. McGraw-Hill, 2005.
- [19] Vincent D. Blondel et al. Fast unfolding of communities in large networks. *J. Stat. Mech.: Theory Exp.*, 2008(10):P10008, 2008.
- [20] Peter J. Rousseeuw. Silhouettes: a graphical aid to the interpretation and validation of cluster analysis. *J. Comput. Appl. Math.*, 20:53–65, 1987.
- [21] Lawrence Hubert and Phipps Arabie. Comparing partitions. *J. Classification*, 2(1):193–218, 1985.
- [22] Tadeusz Nawrot et al. A case study of a small diameter gravity sewerage system in Zolkiewka Commune, Poland. *Water*, 10(10), 2018.
- [23] Fred Sonnenwald et al. Quantifying mixing in sewer networks for source localization. *J. Environ. Eng.*, 149(5):04023019, 2023.